

# A cubesat mission concept for the remote sensing of the Martian atmosphere

Gregor Moeller<sup>1</sup>, Chi O. Ao<sup>2</sup>, and Anthony James Mannucci<sup>3</sup>

<sup>1</sup>ETH Zürich

<sup>2</sup>Jet Propulsion Laboratory

<sup>3</sup>Jet Propulsion Laboratory, California Institute of Technology

November 24, 2022

## Abstract

The atmospheric measurements made by the six Mars orbiters in operation (as of July 2020) significantly improved our understanding of the Martian weather and climate. However, while some of these orbiters will reach their lifetime, innovative and cost-effective missions are requested - not only to guarantee continued observation but also to address potential gaps in the existing observing network. Inspired by the success of the two Mars Cube One (MarCO) satellites we have established a mission concept, which is based on a series of cubesats, carried to Mars and injected into a low-Mars orbit as secondary payload on a larger orbiter. Each cubesat will be equipped with the necessary features for cross-link radio occultation (RO) measurements in X-band. Intelligent attitude control will allow for maintaining the cubesats in a so-called “string-of-pearls” formation over a period of about 150 solar days. During this period, a series of RO experiments will be carried out with the larger orbiter for up to 180 measurement series per day. Due to the specific observation geometry, we will obtain a unique set of globally distributed cross-link occultations. For processing of the observations, tomographic principles are applied to the RO measurements for reconstruction of high-resolution 2D temperature and pressure fields of the lower Martian atmosphere. The obtained products will give an insight into various unresolved atmospheric phenomena - especially of those which are characterized by distinct horizontal gradients in pressure and temperature, e.g. as observed at the day-night terminator, during dust storms, or over complex terrain.

# A cubesat mission concept for the remote sensing of the Martian atmosphere

Gregor Moeller<sup>1,\*</sup>, Chi O. Ao<sup>1</sup>, and Anthony J. Mannucci<sup>1</sup>

<sup>1</sup>NASA Jet Propulsion Laboratory, California Institute of Technology, Pasadena, California, USA

\*now at: ETH Zurich, Institute of Geodesy and Photogrammetry, Zurich, Switzerland

## Key Points:

- The diurnal cycle and meso-scale to small-scale processes in the Martian atmosphere are currently undersampled
- Cubesat based radio occultation measurements can fill in the gaps in the Mars observation network
- Atmospheric tomography is an innovative tool for processing of radio occultation measurements

## Abstract

The atmospheric measurements made by the six Mars orbiters in operation (as of July 2020) significantly improved our understanding of the Martian weather and climate. However, while some of these orbiters will reach their lifetime, innovative and cost-effective missions are requested - not only to guarantee continued observation but also to address potential gaps in the existing observing network. Inspired by the success of the two Mars Cube One (MarCO) satellites we have established a mission concept, which is based on a series of cubesats, carried to Mars and injected into a low-Mars orbit as secondary payload on a larger orbiter. Each cubesat will be equipped with the necessary features for cross-link radio occultation (RO) measurements in X-band. Intelligent attitude control will allow for maintaining the cubesats in a so-called "string-of-pearls" formation over a period of about 150 solar days. During this period, a series of RO experiments will be carried out with the larger orbiter for up to 180 measurement series per day. Due to the specific observation geometry, we will obtain a unique set of globally distributed cross-link occultations. For processing of the observations, tomographic principles are applied to the RO measurements for reconstruction of high-resolution 2D temperature and pressure fields of the lower Martian atmosphere. The obtained products will give an insight into various unresolved atmospheric phenomena - especially of those which are characterized by distinct horizontal gradients in pressure and temperature, e.g. as observed at the day-night terminator, during dust storms, or over complex terrain.

## Plain Language Summary

Satellite missions to Mars are crucial for monitoring the atmospheric state and to derive valuable information about the weather and climate on our red fellow planet. When traveling through the atmosphere, the radio links between orbiting satellites are delayed and the frequency shifts can be used to carefully study the atmospheric processes in detail. However, the existing Mars orbiters are not designed for cross-link measurements between the orbiters and thus, the number of radio observations is limited. In order to overcome current limitations, we present a new mission concept, which is based on four cubesats, deployed into in a so-called "string-of-pearls" formation around Mars. The established constellation will allow for 180 globally distributed measurement series per day and each series opens the ability to study horizontal and vertical structures in the Martian atmosphere with fine resolution. A new processing strategy based on tomographic principles applied to the radio observations will allow to further increase the horizontal resolution. The obtained products will give an insight into various unresolved atmospheric phenomena, e.g. at the day-night terminator, during dust storms or at the edge of the polar ice caps.

## 1 Introduction

Since the very beginning of planetary exploration, communication links between the Earth and spacecraft are used not only for data transfer but also to "examine important properties of planetary atmospheres [...] by carefully studying small changes in the radio signal's frequency" (Asmar et al., 2019) when the spacecraft occults behind the planet. The first radio science experiment through the Martian atmosphere was carried out during the flyby of the Mariner 4 spacecraft in 1965 (Harrington et al., 1968). Since then, almost every mission to Mars, either flyby or orbiter mission, has been used for planetary radio occultation (RO) experiments to obtain a better insight into the atmospheric processes on Mars.

The six Mars orbiters in operation (as of July 2020): Mars Odyssey, Mars Express, Mars Reconnaissance Orbiter, India's Mars Orbiter Mission, Mars Atmosphere and Volatile Evolution Orbiter (MAVEN), and ExoMars Trace Gas Orbiter, are equipped with S-band (2.3 GHz), X-band (8.4 GHz) or Ka-band (31.8 GHz) communication links suited for ra-

63 dio science experiments. Nevertheless, the typical Earth-to-spacecraft geometry for plan-  
 64 etary RO results in limited latitude and local time distribution for the profiles. In ad-  
 65 dition, longer observation gaps appear, e.g. when the orbital plane of the spacecraft is  
 66 perpendicular to the Earth-Mars line or if the Earth-Mars line is too close to the Sun.

67 In order to further increase the number of observations, Ao et al. (2015) have car-  
 68 ried out a series of cross-link occultation experiments using the UHF-band (0.4 GHz) Elec-  
 69 tra transceivers of Mars Odyssey (ODY) and Mars Reconnaissance Orbiter (MRO). The  
 70 UHF communication link is designed for proximity communications with the Mars lan-  
 71 ders and rovers. During regular relay service between ODY and a ground asset, MRO  
 72 was eavesdropping to the UHF signal of ODY and recorded the in-phase and quadra-  
 73 ture components in open-loop tracking mode. The analysis of the phase measurements  
 74 revealed that the signal-to-noise ratio of the received UHF signal and the clock stabil-  
 75 ity is sufficient for RO studies of the electron density in the ionosphere between 50 km  
 76 and 200 km altitude.

77 Motivated by the success of the first cross-link experiments, further cross-link mea-  
 78 surements are being planned, e.g. between Mars Express and the ExoMars Trace Gas  
 79 Orbiter (Hakan Svedhem, personal communication, Sep 2019). Various studies (Asmar  
 80 et al., 2016; Tellmann et al., 2019; Mannucci et al., 2015) confirm that cross-link RO can  
 81 produce high signal-to-noise ratio of the received signal, and further increase the planetary-  
 82 scale distribution of the RO measurements. Though, if cross-link RO purely relies on ex-  
 83 isting Mars orbiters, its full potential cannot be exploited due to the limitations in ra-  
 84 dio frequency and orbital geometry. For example, the single-frequency UHF link does  
 85 not allow for separation of ionospheric and neutral atmospheric effects.

86 The Integration Report from the 9th International Conference on Mars (Yingst et  
 87 al., 2019) highlights current gaps in our knowledge about the diurnal atmospheric cy-  
 88 cle and various meso- to small-scale processes in the lower atmosphere such as gravity  
 89 waves, clouds or other phenomena on short timescales. In order to guarantee continued  
 90 observation about the Martian atmospheric state and to close potential gaps in the ex-  
 91 isting observing network in a cost effective way, small-satellite missions seem to be an  
 92 ideal candidate. Inspired by the success of the two Mars Cube One (MarCO) spacecraft  
 93 (Klesh & Krajewski, 2015; Asmar & Matousek, 2016) and the widening use of small satel-  
 94 lites for GNSS RO for sensing the Earth’s atmosphere, we present a new mission con-  
 95 cept which addresses the current limitations. In Section 2 the general mission concept  
 96 is outlined. Section 3 highlights details about the spatio-temporal distribution of the ex-  
 97 pected observations. Section 4 provides more details about the processing of the RO sig-  
 98 nals using tomographic principles. The tomography case study itself is described in Sec-  
 99 tion 5. A conclusion and outlook will be provided in Section 6.

## 100 2 Mission Concept

101 The proposed mission concept is based on four cubesats and a main orbiter, which  
 102 deploys the cubesats into a dense local constellation during aerobraking. The use of RO  
 103 cubesats flying in close formation has recently been proposed for an Earth observation  
 104 concept (Turk et al., 2019). The advantage from such configuration is that we can get  
 105 simultaneous RO observations that are closely located. Although the mission concept  
 106 is not particularly dependent on a specific main orbiter, we selected ESA’s Mars Sam-  
 107 ple Return (MSR) orbiter (Joffe et al., 2018) as a potential candidate - primarily be-  
 108 cause detailed aerocapture studies for cubesats are not available yet and the MSR or-  
 109 biter would be one of the next possibilities to deploy cubesats into a low Mars orbit.

110 Based on the intended orbital elements of the main orbiter (see Table 1), we de-  
 111 veloped a deployment plan, which is illustrated in Figure 1. For the four cubesats, we  
 112 suggest a so-called ”string-of-pearls” formation (Tan et al., 2002). It provides the nec-

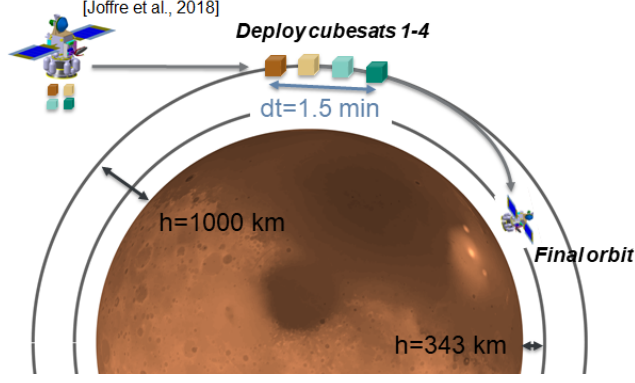


**Figure 1.** Overview of the cubesat deployment. The four cubesats are carried to Mars by a main orbiter and deployed into a so-called string-of-pearls formation

**Table 1.** Orbital elements of the main orbiter and the four cubesats

Spacecraft	h [km]	i [deg]	$M_0$ [deg]	e	$\dot{\Omega}$ [deg/sol]	Period (hh:mm)
main orbiter	343	60	0	0.0	-5.2 <sup>a</sup>	01:55
cubesats 1-4	1000	60	0, 1.2, 2.4, 3.6	0.0	-3.2 <sup>a</sup>	02:27

<sup>a</sup> Nodal precession rate  $\dot{\Omega}$  according to Eq. 1

essary observation geometry for sensing meso- to small-scale structures in the Martian atmosphere (see Section 3 for details). After deployment of the cubesats, the main orbiter carries out a series of maneuvers to reach its final orbit. The radio link between main orbiter and each of the four cubesats can be used to provide RO measurements. In the following, the orbit geometry and the individual components of the observation concept are described in detail.

## 2.1 Selection of Orbits

The orbital elements of the main orbiter are based on the numbers provided by Joffre et al. (2018), except for the inclination. Instead of  $40deg$  we propose an inclination of  $60deg$ , which enables nearly global coverage for limb sounding and a reasonable nodal precession rate ( $\dot{\Omega}$ )

$$\dot{\Omega}(a, i) = \frac{-3}{2} \cdot n \cdot J_2 \cdot \frac{R^2}{(a \cdot (1 - e^2))^2} \cdot \cos(i), \quad (1)$$

where  $n = \sqrt{GM/a^3}$  is the mean motion of the spacecraft,  $a = R+h$  is the semi-major axis,  $e$  is the eccentricity and  $i$  is the inclination of the orbital plane, with  $GM = 42828.375214 km^3/s^{-2}$  and  $R = 3389.5 km$ . The term  $J_2 = 1.96045 \cdot 10^{-3}$  of the geopotential compensates for the non-sphericity of Mars (higher order terms are not considered). Assuming a spacecraft altitude of  $343 km$  and an inclination of  $60deg$ , the nodal precession of the main orbiter works out to be  $-5.2 deg/sol$  (solar day on Mars).

For the four cubesats, we assume the same inclination as for the main orbiter, since a change of inclination requires a large amount of delta v (change in the orbiter vector velocity). Besides, we propose an altitude of  $1000 km$  (orbital period of 2 h 27 min), which is not in resonance with the rotation rate of Mars ( $24.659722 h/rev$ ) and therefore, guarantees good longitudinal coverage. The resulting nodal precession of the cubesats is  $-3.2 deg/sol$ .

The spacing between the cubesats is set to  $dM = 1.2deg$ . At an altitude of  $1000km$  this equals to a temporal spacing of about  $30sec$ . For the mission concept, the cubesat spacing is an important parameter. It defines not only the time between the RO measurements but also the observation geometry, i.e. the horizontal resolution and area covered (see Section 3 for further details). Over the minimum lifetime of 150 solar days (see Section 3), we expect that the four cubesats can be kept in formation with minor orbital corrections. Therefore, one possibility would be the use of an intelligent attitude control system using solar radiation pressure forces (Kumar et al., 2014). Assuming a six-unit cubesat with deployable  $30cm \times 30cm$  solar panels (as used for the two MarCO spacecraft), the maximum and minimum area pointing in direction of the Sun may vary from  $0.05m^2$  to  $0.15m^2$ , respectively. This will cause an acceleration due to solar radiation pressure of about  $9 \cdot 10^{-9}ms^{-2}$  to  $3 \cdot 10^{-8}ms^{-2}$ , assuming a solar radiation pressure coefficient of 1.3 and a satellite mass of  $13.5kg$ . After one revolution, this leads to a potential correction of the cubesat orbit of a few meters. This small correction could be essential for formation maintenance by compensating the remaining atmospheric drag or higher order gravitational anomalies. In contrast, the orbital drift of the main spacecraft is less critical, i.e. a change of the orbital elements of the main orbiter due to gravitational and non-gravitational forces has little impact on the observation geometry.

## 2.2 Observation Concept

The RO technique is an active sounding technique that requires stable frequency reference on both the transmitter and the receiver ends. In the following, we will distinguish two possible observation scenarios.

Scenario 1: Two-way RO experiment. The main orbiter is equipped with an X-band radio, e.g. IRIS radio (Kobayashi et al., 2019), with 4 receive and transmit ports and an Ultra Stable Oscillator (USO, Allan Dev:  $10^{-13}/100s$ ). Each cubesat provides dual-frequency signal relay only (requires less complex cubesat design), either in X-band or Ka-band, which allows for the separation of ionospheric and neutral atmospheric effects - as already successfully applied for Mars Express orbiter, see (Pätzold et al., 2004).

Scenario 2: Dual one-way RO experiment (active cubesats). Each satellite is equipped with a dual-frequency radio (e.g. a modified version of the IRIS radio). Both, main orbiter and cubesats will transmit simultaneously in slightly different frequency bands. As a consequence, the clock error can be largely canceled out in post-processing. The different frequency bands are used so that hardware filters can prevent the sensitive receive module from being saturated by leakage from the transmit antenna.

Figure 2 highlights the system architecture of the dual one-way concept. The observable is the result of summing the phases measured by the two receivers, one on vehicle A and the other on vehicle B. The summation occurs in post-processing in the science data system. In contrast to scenario 1, where a USO is required to reduce the impact of the clock error term, the stability of the clock can be relaxed since what enters into the retrieval error is clock error variation over the time it takes for the signal to travel between the two spacecraft (see Appendix A for a mathematical description). Given the typical light travel time of  $0.01sec$  between the two spacecraft during an occultation, clock stability of  $\sim 10^{-11}$  is sufficient to provide the same clock performance of an USO (though at the expense of a  $\sqrt{2}$  increase in thermal noise).

In addition to the RO measurements, the established link between main orbiter and cubesats is used for the determination of the cubesat orbits. According to Williamson et al. (2017) the orbit errors during the RO event can be minimized if the necessary observations are scheduled directly before or after the cubesat is occulting. In order to resolve a frequency shift of  $0.01Hz$  (like for the Mars Global Surveyor radio occultation experiment, see Hinson et al. (1999)) in X-band caused by atmospheric refraction, the line-

of-sight velocity between main orbiter and cubesat has to be known with an accuracy of about  $0.5\text{mm/s}$ .

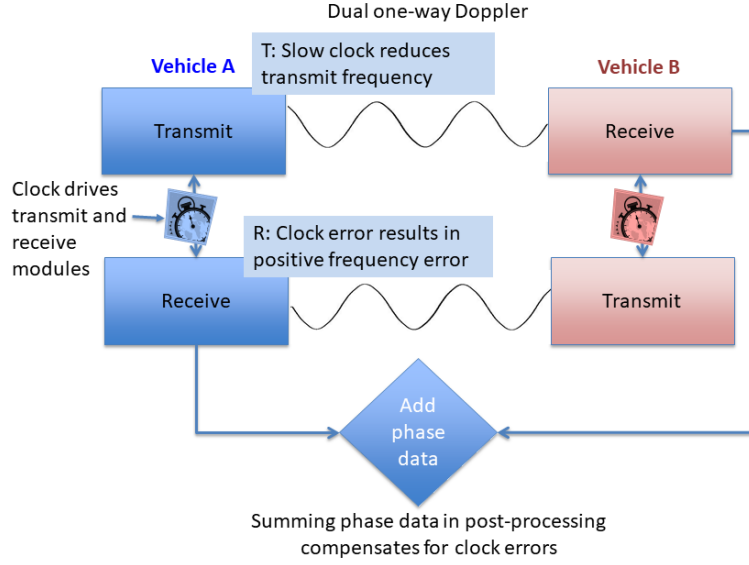


**Figure 2.** System architecture of the dual one-way observation concept

### 3 Spatio-temporal Distribution of Observations

Based on the orbital elements listed in Table 1, all possible cross-link radio occultation events between main orbiter and the four cubesats have been identified. In the following, the results are shown for a period of 150 sols (about 5 months). This period reflects approximately the duration of the 2018 global dust storm, which lasted from May to September 2018. Due to nodal precession, this is also the time needed to reach again the same orbit configuration ( $2.4\text{ deg/sol}$  relative drift between orbital planes), i.e. covers the possible observation geometries.

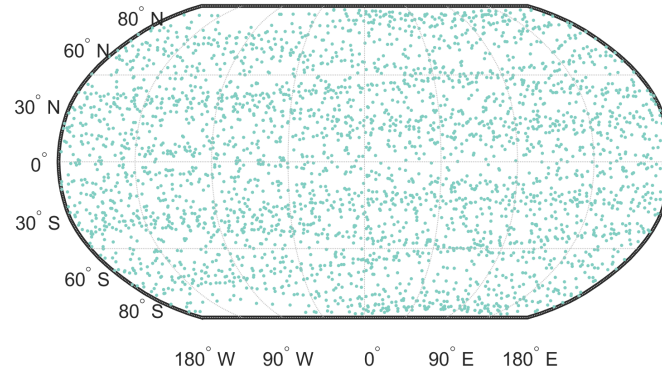


**Figure 3.** Global distribution of radio occultation events as expected between main orbiter and each cubesat over a period of 150 sols. Each dot represents the tangent point of a RO event, i.e. the point where the signal grazes the surface of Mars

Figure 3 shows the global distribution of the 3200 RO events as identified between main orbiter and cubesat 1 over the period of 150 sols. Due to the limb sounding geometry, a full global distribution can be obtained in which not only the latitude bands between  $60\text{ deg S}$  and  $60\text{ deg N}$  are covered (as expected from the inclination of the orbits) but also the polar regions up to  $85\text{ deg}$  latitude. A similar distribution is expected between the main orbiter and the other three cubesats. Due to the relatively close spacing, no occultation measurements are possible between the cubesats themselves. However, in the following it is shown why this configuration is beneficial.

The angle between the two orbital planes (main orbiter and cubesats 1-4) is constantly changing due to nodal precession. In consequence, the number of observations per sol, their global distribution but also the observation geometry of the RO events change too. In order to characterize the observation geometry and to better understand the temporal variations, in the following we will distinguish between two scenarios. In the first scenario, the orbital planes are perpendicular to each other and radio occultation measurements are obtained in cross-track direction. In consequence, from the four cubesats in formation we obtain four ray paths which are widely parallel to each other, see Figure 4 left. In the second scenario (about 35 sols later) the orbital planes are aligned. As a consequence, radio occultation measurements are obtained in flight direction. This provides a unique observation geometry, in which consecutive observations overlap, see Figure 4 right. With these two configurations the distribution of observations is explained. All other cases can be described as a combination of the two scenarios.

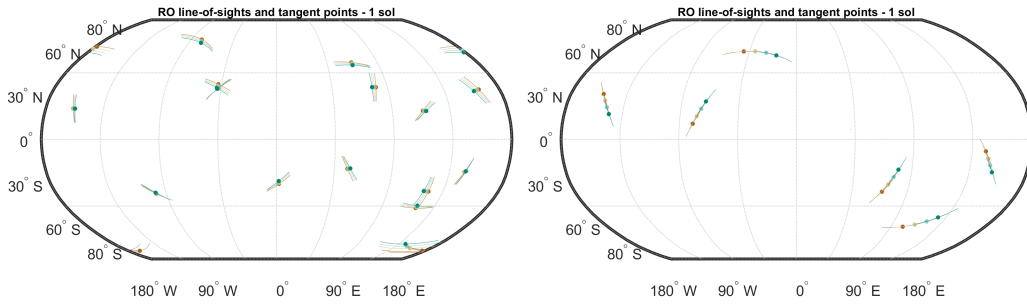


**Figure 4.** Geometry and distribution of RO events - exemplary for two solar days on Mars. The left plot results from a  $90\text{ deg}$  angle between the orbital planes. The right plot is obtained, if the orbital planes are aligned. Each line represents a ray path between main orbiter and one cubesat, each dot the corresponding RO tangent point.

In total, from the four cubesats we expect 20 to 180 cross-link ROs per day, which is substantially more than currently recorded by six operational orbiters in the typical Earth-spacecraft geometry. The varying number of events is explained by the changing observation geometry over the course of 150 sols. In case of aligned orbits (see Figure 4 right), all spacecraft fly in common directions with similar speed. This leads to a temporal clustering of RO events and longer observation gaps between the clusters.

According to Figure 4, the clustering of RO events seems to be beneficial for sensing of meso- to small-scale structures in the atmosphere. Especially due to the small temporal spacing of the four cubesats of about  $30\text{ sec}$  nearby regions in the atmosphere can be sensed almost simultaneously. In Figure 5, the spatio-temporal separation of consecutive ROs is highlighted - exemplary for the first two cubesats. Over the course of 150 sols, the time between two consecutive ROs varies between a few seconds, but can be up to  $100\text{ sec}$ . In consequence, the horizontal distance between the tangent points varies significantly - for the proposed constellation between  $30\text{ km}$  in case of perpendicular orbits,



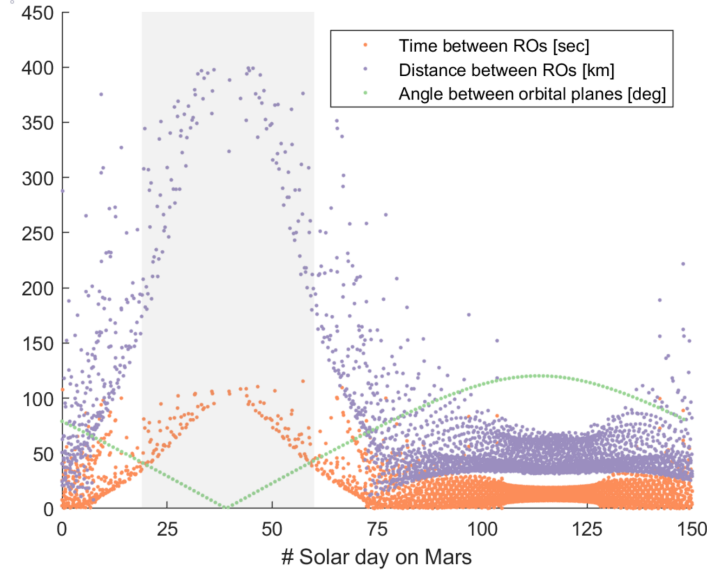


**Figure 5.** Selected parameters describing the clustering of RO events. In case cubesat 1 becomes visible at the horizon, the "Time between ROs [sec]" indicates how long it takes until the second cubesat becomes visible for the main orbiter. The "Distance between ROs [km]" describes the horizontal distance between the RO events of cubesat 1 and 2.

up to  $400\text{km}$  in case of aligned orbits. In addition, we analyzed also the temporal resolution as seen by an observer on Mars (not presented here). It turned out, that with the suggested constellation we are sensitive to the diurnal cycle. It lasts about 40 sols until the entire diurnal cycle is covered - a reasonable time to decorrelate sub-daily atmospheric effects from seasonal variations (Kursinski et al., 2004).

## 4 Processing Strategy for Cross-link Occultations

The frequency residuals, as expected from cross-link occultations between main orbiter and the four cubesats in formation, allow for computation of the atmospheric state variables (pressure and temperature) along the path of signal propagation. However, the processing is not straight forward, but requires ancillary information (e.g. satellite ephemerides) and is based on assumptions concerning signal propagation and the atmospheric strata.

### 4.1 Conventional Retrieval Method

Ignoring diffraction effects and assuming spherical atmospheric symmetry, the one-way or two-way frequency residuals may be processed using the Abel transform to obtain vertical profiles of index of refraction (Fjeldbo et al., 1971; Hinson et al., 1999; Withers et al., 2014), which can be further converted into temperature and pressure. Applied to cross-link occultations, this method will lead to vertical profiles of pressure and temperature with a resolution of about  $500\text{m}$  (limited by the Fresnel-scale) and thus, will not only provide a better insight into the vertical atmospheric structure during all local times but also into horizontal structures smaller than a few hundred kilometers - realized by the small separation of the cubesats (see Figure 5).

## 4.2 Tomography Processing

In order to overcome the limitations of the Abel transform - especially the symmetry assumption - and to further increase the horizontal resolution, we propose a new processing strategy which is based on tomographic principles. As shown in the following, tomographic principles are well suited for the processing of "clustered" RO measurements, as expected from dense cubesat formations. According to Iyer and Hirahara (1993), the general principle of tomography is described as follows:

$$f_s = \int_S g(s) \cdot ds \quad (2)$$

where  $f_s$  is the projection function,  $g(s)$  is the object property function and  $ds$  is a small element of the ray path  $S$  along which the integration takes place. For the processing of radio occultation data,  $g(s)$  is replaced by index of refraction  $n$  and  $f_s$  is the signal phase delay ( $dL$ ). If Doppler shift ( $df$ ) is provided instead of phase delay, with sampling rate  $dt$ , it can be converted as follows:

$$dL = \sum_i \Delta dL(i) \quad (3)$$

with

$$\Delta dL(i) = -\frac{df(i)}{1 + f_t/f_r} \cdot \frac{c}{f_r} \cdot dt. \quad (4)$$

In Eq. 4, the correction term ( $f_t/f_r$ ) has to be applied if the received frequency ( $f_r$ ) differs from the transmitted frequency ( $f_t$ ), e.g. if the transmitted signal is multiplied with a certain ratio before re-transmission, which is beneficial in the two-way RO concept. In any case, the ionospheric effect on the Doppler shift has to be corrected beforehand using dual-frequency observations or ionospheric models like the one described by Pi et al. (2008). The resulting basic function of tomography reads:

$$dL = \int_S n \cdot ds - \int_{S_0} ds \quad (5)$$

where  $S$  is the "true" signal path and  $S_0$  is the theoretical straight line signal path in vacuum.

One difficulty in performing the first integral in Eq. 5 is that the ray path is not a straight line but rather dependent on the object properties along the signal path. A change in  $n$  leads to a change in  $S$  and  $f_s$ . However, from Fermat's principle it can be assumed that first order changes of the ray path lead to second order changes in travel time, i.e. for small perturbation of the path, the travel-time is stationary. In fact, we make use of this principle for setting up the tomography approach. The resulting "non-linear" approach ignores the path-dependency in the inversion of  $n$  along  $ds$  but takes the signal bending into account by the definition of the ray paths. In consequence, the tomography solution is derived iteratively. After each processing step the ray paths are re-computed by solving the Eikonal equation using, e.g. ray-tracing shooting techniques, see Moeller and Landskron (2019).

In order to find a numerical solution for Eq. 5, the object of interest, e.g. the neutral atmosphere is discretized in area elements (in two-dimensions) in which the index of refraction is assumed as constant. Consequently and by replacing the index of refraction with refractivity  $N = (n - 1) \cdot 10^6$ , Eq. 5 reads:

$$dL = 10^{-6} \sum_{k=1}^m N_k \cdot d_k \quad (6)$$

where  $N_k$  is the refractivity and  $d_k$  is the ray length in area element  $k$ .

**Table 2.** Tomography settings applied for the reconstruction of refractivity fields from (simulated) cross-link RO observations

Parameter	Settings
Case study domain	High northern latitudes (40 – 80 deg $N$ )
Case study period	Late autumn ( $L_s = 270$ deg)
Model resolution	60km (horizontally) $\times$ 1km (vertically)
Tomography software	Modified version of ATom software package*
Initial field	Mars GRAM model (Justus et al., 2002)
Inversion method	Singular value decomposition ( $eigenv_{min} = 0.01km^2$ )
Estimation method	Iterative weighted least squares adjustment
Convergence criteria	RMS of weighted residuals

\* <https://github.com/GregorMoeller/ATom>

In case of overlapping signal paths (e.g. in case of aligned orbital planes) a linear equation system can be set up for the reconstruction of the refractivity along the signal paths. In matrix notation it reads:

$$\mathbf{dL} = \mathbf{A} \cdot \mathbf{N} \quad (7)$$

where  $\mathbf{dL}$  is the observation vector,  $\mathbf{N}$  is the vector of unknowns and  $\mathbf{A}$  is a matrix which contains the spatial derivatives of the observations with respect to the unknowns, i.e. the ray lengths ( $d_k$ ) in each area element. For determining the unknown vector  $\mathbf{N}$ , the inverse  $\mathbf{A}^{-1}$  must to be formed. However, in most cases matrix  $\mathbf{A}$  is not of full rank, thus regularization methods have to be applied to determine the pseudo inverse. Therefore, we make use of truncated singular value decomposition methods as described by Strang and Borre (1997) and Moeller (2017).

## 5 Tomography Case Study

For technique demonstration, a closed-loop simulation was carried out using planetWRF (Richardson et al., 2007) - a modified version of the Weather Research and Forecasting (WRF) model for planetary atmospheres - to simulate the atmospheric state along the RO signal paths of the proposed cubesat-orbiter constellation. The model data used are atmospheric pressure and temperature, provided on a global  $5\text{ deg} \times 5\text{ deg}$  grid for 40 vertical layers, with a 3-hour temporal resolution. In a first step, the signal paths through the atmosphere were reconstructed every 500ms using ray-tracing shooting techniques (Moeller & Landskron, 2019) with a step size of 1km. Since atmospheric density is exponentially decreasing with altitude, refractivity  $N$  was computed for signals penetrating into the lower 50km of the atmosphere only. The simulated refractivities along the RO signal paths were converted into phase delays using Eq. 6 and the area covered by the observations was parametrized in area elements with a grid size of 60km (horizontally)  $\times$  1km (vertically). Figure 6 shows the observation geometry together with the ray paths through the simulated refractivity field. For the case study, only observations with an azimuth angle less than 25 deg were simulated. For these observations tomographic principles are most beneficial - mainly due to overlapping signal paths (see Figure 4 right). The tomographic processing itself, i.e. the estimation of refractivity fields from phase measurements, was carried out using a modified version of the ATom software package (Moeller, 2017). Table 2 summarizes the major settings.

For visualization and validation against WRF, the tomography derived refractivity fields were converted into atmospheric pressure and temperature, assuming hydrostatic equilibrium and an initial temperature of 220K at 50km altitude. Figure 7 shows

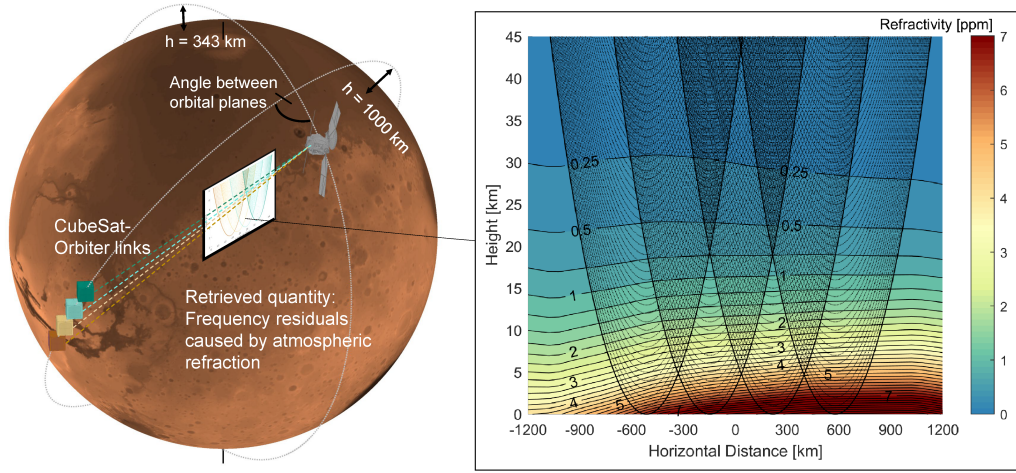


**Figure 6.** Left: Observation geometry for cross-link occultations. Right: The planetWRF (Richardson et al., 2007) derived refractivity field along the RO signal paths

the resulting temperature field and temperature differences for a case study in high northern latitudes ( $40 - 80 \text{ deg } N$ ) in late autumn ( $L_s = 270 \text{ deg}$ ). The WRF-based temperature field is characterized by strong vertical inversions and distinct negative horizontal temperature gradients in direction of the North Pole. According to Tellmann et al. (2013), the strong temperature gradients are associated with strong zonal jets in the Martian winter hemisphere and adiabatic heating in the subsiding branch of the Hadley circulation. These temperature structures are very well resolvable by the proposed cubesat formation and processing of the RO signals using tomographic principles.

For the tomography derived temperature field, a RMSE of  $6.5K$  and a bias of  $0.5K$  was obtained for the lowest  $30km$  of the atmosphere. Above, the RMSE increases - mainly due to temperature initialization problems. Overall, the best solution was obtained within the horizontal range  $[-600km, 600km]$  in which multiple observations overlap (see Figure 6 right) and therefore, help to further stabilize the tomography solution. The RMSE in this "core" domain of the tomography model is about  $3.5K$ , and therefore, by a factor of 2-3 better than in the outer regions.

## 6 Conclusions and Outlook

In this study, we address the basic components of a cubesat mission to Mars for remote sensing of the Martian atmosphere using the radio occultation technique. In an optimization process we have identified a circular low-Mars orbit with an inclination of about  $60 \text{ deg}$  as beneficial for deployment of the cubesats. However, detailed aerocapture studies for cubesats are not available yet. Hence, the final deployment plan will depend on the spacecraft that will be selected as transit vehicle for the cubesats to Mars.

The goals of this mission is to provide valuable measurements about the diurnal cycle and various meso- to small-scale processes in the lower Martian atmosphere. Both have been identified by the Integration Report from the 9th International Conference on Mars (Yingst et al., 2019) as the major gaps in the current Martian observing network. In order to fulfill the mission goal, four cubesats in a so-called string-of-pearls formation have been identified as minimum requirement. The challenge will be to maintain such kind of formation over a period of 150 solar days at least - if needed without

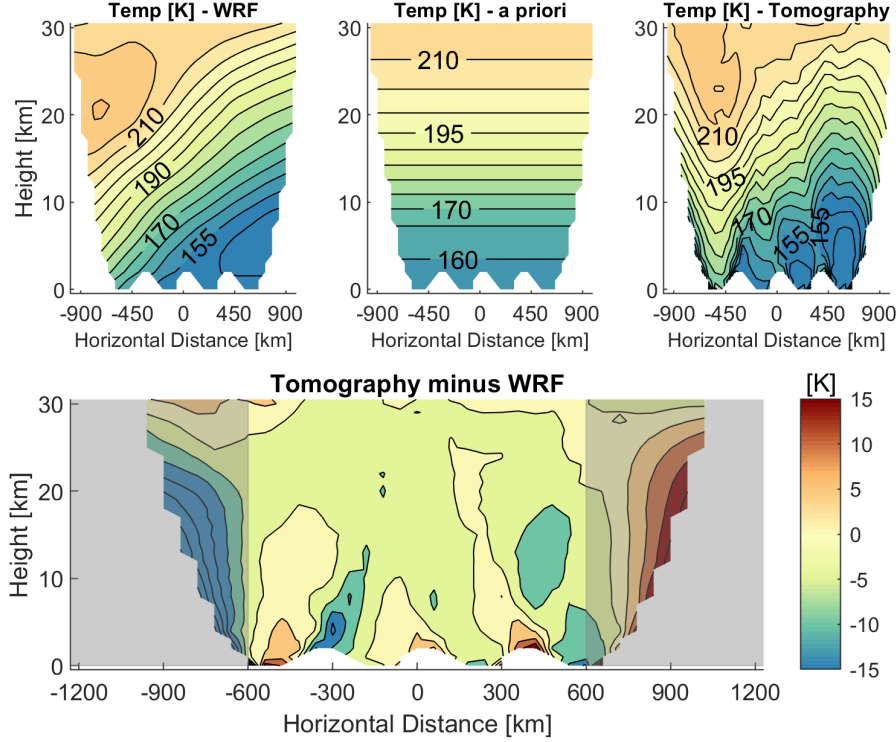


**Figure 7.** Top left: planetWRF temperature field for high northern latitudes in late autumn (reference). Top middle: Symmetric a priori field derived from Mars GRAM model. Top right: Estimated temperature field using tomographic principles. Bottom: Closed-loop validation (Tomography minus WRF) to assess the performance of the tomography approach under rather realistic atmospheric conditions

active propulsion systems. The details of orbit control, e.g. using an intelligent attitude control system, have to be examined in further studies.

For realization of the occultation measurements, a dual one-way observation concept is foreseen between the cubesats and the main orbiter. The advantage of this observation concept is lower demands on the frequency stability but requires a dual-frequency radio on both sides, and active cubesats for signal tracking and data transfer to the main orbiter - or any communication satellite for data transfer to the Earth. However, the data rate per satellite pair seems to be less critical. According to our simulations, each satellite pair will generate about *2Mb* of data per day, including radio occultation and additional range measurements for orbit determination.

In a number of close-loop validations, the expected observations but also possible processing strategies have been evaluated. Due to the unique observation geometry, a combined processing of the radio occultation measurements using tomographic principles seems to be promising and allow to further increase the horizontal resolution of the reconstructed temperature and pressure fields. In addition, tomographic principles are not based on spherical symmetric assumption and thus, allow for resolving distinct temperature gradients and inversion layers in the lower Martian atmosphere. In the conducted tomography case study, we have identified a core domain in which an accuracy in temperature of a few Kelvin is achieved. The extent of the domain but also the tempera-

ture accuracy might be further increased by additional cubesats added to the proposed constellation.

## Appendix A Mathematical derivation of the dual one-way concept

In the following we show mathematically how the dual one-way configuration leads to reduction of the effects of clock error.

The transmitted phase from vehicle A at frequency  $f_a$  and at time  $\tau_0$  is given by  $\Phi_a^T(\tau_0)$ . The received phase at vehicle B, accounting for various forms of delay along the path between vehicles A and B, can be written as:

$$\begin{aligned} \phi_b(\tau_0 + \rho/c + d/c + I_a/c) = & \Phi_a^T(\tau_0) + \nu_a + (\rho/\lambda_a) + (d/\lambda_a) + (I_a/\lambda_a) \\ & + c_a(\tau_0)f_a - c_b(\tau_0 + \rho/c + d/c + I_a/c)f_a + \mu_b \end{aligned} \quad (\text{A1})$$

where we have defined the following distances, clock terms, frequencies and noise terms as:

$\rho$  = geometric range between the vehicles

$d$  = phase delay due to atmosphere

$I_a$  = phase delay due to ionosphere, at A's transmit frequency  $f_a$

$c_a(\tau_0)$  = clock error at vehicle A in seconds, at time  $\tau_0$

$c_b(\tau_0 + \rho/c + d/c + I_a/c)$  = clock error at vehicle B, at the receive time

$\lambda_a$  = wavelength of A's transmit frequency

$\nu_a$  = phase noise on A's transmitter

$\mu_b$  = phase noise on B's receiver

where analogous quantities are defined for vehicle B which transmits at frequency  $f_b$ . We can similarly write the received phase at vehicle A as:

$$\begin{aligned} \phi_a(\tau_0 + \rho/c + d/c + I_b/c) = & \Phi_b^T(\tau_0) + \nu_b + (\rho/\lambda_b) + (d/\lambda_b) + (I_b/\lambda_b) \\ & + c_b(\tau_0)f_b - c_a(\tau_0 + \rho/c + d/c + I_b/c)f_b + \mu_a \end{aligned} \quad (\text{A2})$$

If we add the measured phases  $\phi_a$  and  $\phi_b$  in post-processing, we can derive the following expression for the atmospheric delay  $d$ :

$$\begin{aligned} d = & \frac{\lambda_a \lambda_b}{\lambda_a + \lambda_b} (\phi_a + \phi_b - \Phi_a^T(\tau_0) - \Phi_b^T(\tau_0) \\ & + [c_b(\tau_0 + \delta t)f_a - c_b(\tau_0)f_b] + [c_a(\tau_0 + \delta t)f_b - c_a(\tau_0)f_a]) \end{aligned} \quad (\text{A3})$$

where we have neglected noise terms and assumed that geometric delay and ionospheric delay are removed in post-processing. We have isolated the two nearly-cancelling clock terms as the final two bracketed expressions. The term  $\delta t$  now represents the transit time for the signal between vehicles A and B.



## Acknowledgments

This work was performed at the Jet Propulsion Laboratory, California Institute of Technology, under a contract with National Aeronautics and Space Administration (NASA). Gregor Moeller's research was supported by an appointment to the NASA Postdoctoral Program at NASA Jet Propulsion Laboratory, administered by Universities Space Research Association under contract with NASA. The authors gratefully acknowledge Michael A. Mischna (NASA, JPL) for providing the planetWRF data.

## References

- Ao, C. O., Edwards, C. D., Kahan, D. S., Pi, X., Asmar, S. W., & Mannucci, A. J. (2015). A first demonstration of Mars crosslink occultation measurements. *Radio Science*, 50(10), 997–1007. doi: 10.1002/2015RS005750
- Asmar, S. W., Ao, C. O., Edwards, C. D., Kahan, D. S., Pi, X., Paik, M., & Mannucci, A. J. (2016, Mar). Demonstration of Mars crosslink occultation measurements for future small spacecraft constellations. In *2016 IEEE Aerospace Conference* (pp. 1–6). doi: 10.1109/AERO.2016.7500729
- Asmar, S. W., Lazio, J., Atkinson, D. H., Bell, D. J., Border, J. S., Grudin, I. S., ... Preston, R. A. (2019). Future of Planetary Atmospheric, Surface, and Interior Science Using Radio and Laser Links. *Radio Science*, 54(4), 365–377. doi: 10.1029/2018RS006663
- Asmar, S. W., & Matousek, S. (2016). Mars Cube One (MarCO) - shifting the paradigm in relay deep space operation. In *SpaceOps 2016 Conference*. doi: 10.2514/6.2016-2483
- Fjeldbo, G., Kliore, A. J., & Eshleman, V. R. (1971). The Neutral Atmosphere of Venus as Studied with the Mariner V Radio Occultation Experiments. *The Astronomical Journal*, 76(2), 123. doi: 10.1086/111096
- Harrington, J. V., Grossi, M. D., & Langworthy, B. M. (1968). Mars Mariner 4 Radio Occultation Experiment: Comments on the uniqueness of the results. *Journal of Geophysical Research*, 73(9), 3039–3041. doi: 10.1029/JA073i009p03039
- Hinson, D. P., Simpson, R. A., Twicken, J. D., Tyler, G. L., & Flasar, F. M. (1999). Initial results from radio occultation measurements with Mars Global Surveyor. *Journal of Geophysical Research: Planets*, 104(E11), 26997–27012. doi: 10.1029/1999JE001069
- Iyer, H., & Hirahara, K. (1993). *Seismic Tomography: Theory and practice*. Springer Netherlands.
- Joffe, E., Derz, U., Perkinson, M.-C., Huesing, J., Beyer, F., & Sanchez Perez, J.-M. (2018, Nov). Mars Sample Return: Mission analysis for an ESA Earth Return Orbiter. In *7th International Conference on Astrodynamics Tools and Techniques (ICATT)* (pp. 1–15).
- Justus, C. G., James, B. F., Bougher, S. W., Bridger, A. F. C., Haberle, R. M., Murphy, J. R., & Engel, S. (2002). Mars-GRAM 2000: A Mars atmospheric model for engineering applications. *Advances in Space Research*, 29(2), 193–202. doi: 10.1016/S0273-1177(01)00569-5
- Klesh, A., & Krajewski, J. (2015). MarCO: CubeSats to Mars in 2016. In *Proceedings of 29th Annual AIAA/USU Conference on Small Satellites*.
- Kobayashi, M. M., Holmes, S., Yarlagadda, A., Aguirre, F., Chase, M., Angkasa, K., ... Satorius, E. (2019). The Iris Deep-Space Transponder for the SLS EM-1 Secondary Payloads. *IEEE Aerospace and Electronic Systems Magazine*, 34(9), 34–44. doi: 10.1109/MAES.2019.2905923
- Kumar, K. D., Misra, A. K., Varma, S., Reid, T., & Bellefeuille, F. (2014). Maintenance of satellite formations using environmental forces. *Acta Astronautica*, 102, 341–354. doi: 10.1016/j.actaastro.2014.05.001
- Kursinski, E. R., Folkner, W., Zuffada, C., Walker, C., Hinson, D., Ingersoll, A., ...

- Taylor, F. (2004). The Mars Atmospheric Constellation Observatory (MACO) Concept. In G. Kirchengast, U. Foelsche, & A. K. Steiner (Eds.), *Occultations for Probing Atmosphere and Climate* (pp. 393–405). Springer Berlin Heidelberg. doi: 10.1007/978-3-662-09041-1\_35
- Mannucci, A. J., Ao, C. O., Asmar, S., Edwards, C. D., Kahan, D. S., Paik, M., ... Williamson, W. (2015, December). Crosslink Radio Occultation for the Remote Sensing of Planetary Atmospheres. *AGU Fall Meeting 2015*.
- Moeller, G. (2017). *Reconstruction of 3D wet refractivity fields in the lower atmosphere along bended GNSS signal paths* (PhD thesis). TU Wien, Department of Geodesy and Geoinformation.
- Moeller, G., & Landskron, D. (2019). Atmospheric bending effects in GNSS tomography. *Atmospheric Measurement Techniques*, 12(1), 23–34. doi: 10.5194/amt-12-23-2019
- Pätzold, M., Neubauer, F., Carone, L., Hagermann, A., Stanzel, C., Häusler, B., ... Dehant, V. (2004). MaRS: Mars express orbiter radio science. In A. Wilson & A. Chicarro (Eds.), *Mars Express: The Scientific Payload* (pp. 141–163). ESA Spec. Publ., Noordwijk, Netherlands.
- Pi, X., Edwards, C., Hajj, G., Ao, O., Romans, L., Callas, J., ... Kahan, D. (2008, 08). A Chapman-Layers Ionospheric Model for Mars. *NASA STI/Recon Technical Report N*.
- Richardson, M., Toigo, A., & Newman, C. (2007). PlanetWRF: A general purpose, local to global numerical model for planetary atmospheric and climate dynamics. *J. Geophys. Res.*, 112. doi: 10.1029/2006JE002825
- Strang, G., & Borre, K. (1997). *Linear Algebra, Geodesy, and GPS*. Wellesley-Cambridge Press.
- Tan, Z., Bainum, P. M., & Strong, A. (2002). The implementation of maintaining constant distance between satellites in coplanar elliptic orbits. *The Journal of Astronautical Sciences*, 50, 53–69.
- Tellmann, S., Pätzold, M., Häusler, B., Bird, M. K., Hinson, D. P., Andert, T. P., ... Asmar, S. W. (2019, July). Crosslink Occultations for Probing the Planetary Atmosphere and Ionosphere of Mars. *EPSC-DPS Joint Meeting 2019*, 2089.
- Tellmann, S., Pätzold, M., Häusler, B., Hinson, D., & Tyler, G. (2013). The structure of Mars lower atmosphere from Mars Express Radio Science (MaRS) occultation measurements. *J. Geophys. Res. Planets*, 118, 306–320. doi: 10.1002/jgre.20058
- Turk, F. J., Padulles, R., Ao, C. O., de la Torre Juarez, M., Wang, K.-N., Franklin, G. W., ... Neelin, J. D. (2019). Benefits of a Closely-Spaced Satellite Constellation of Atmospheric Polarimetric Radio Occultation Measurements. *Remote Sensing*, 11(20). doi: 10.3390/rs11202399
- Williamson, W., Mannucci, A. J., & Ao, C. O. (2017). Radio occultation mission to Mars using cubesats. In *Proceedings of the Low-Cost Planetary Missions Conference 2017*.
- Withers, P., Moore, L., Cahoy, K., & Beerer, I. (2014). How to process radio occultation data: 1. From time series of frequency residuals to vertical profiles of atmospheric and ionospheric properties. *Planetary and Space Science*, 101, 77–88. doi: 10.1016/j.pss.2014.06.011
- Yingst, R. A., Forget, F., Calvin, W., Des Marais, D., & Niles, P. (2019). *Integration Reports from the Ninth International Conference on Mars* (Tech. Rep.). Retrieved from <https://www.hou.usra.edu/meetings/ninthmars2019/Presentations/Integration.Report.pdf>